A permanent-magnet Zeeman slower and magneto-optical trap for calcium atoms for ultracold Rydberg physics

E. Marin-Bujedo,[1] J.A.L. Grondin,[1,2] T. Schiltz,[1] T. Corbo,[1] X. Urbain,[1] and M. Génévriez[1, a)]
[1)] *Université catholique de Louvain, Institute of Condensed Matter and Nanosciences Chemin du Cyclotron 2, 1348 Louvain-la-Neuve, Belgium*
[2)] *Katholieke Universiteit Leuven, Instituut voor Kern- en Stralingsfysica Celestijnenlaan 200, 3001 Heverlee, Belgium*

(Dated: 16 January 2026)

We report the construction and characterization of an experimental setup for producing a cold gas of ^{40}Ca atoms and excite them to high Rydberg states with a resonant three-photon-excitation scheme. The apparatus comprises four stages, each designed in-house. An oven heated to ~ 500°C generates an atomic beam that is collimated by a capillary stack. The beam is sent into a passive, permanent-magnet-based Zeeman slower that reduces the atomic velocity to 30 m/s. The slow atoms are captured in a magneto-optical trap (MOT) and cooled to 1.0(3) mK with a trapping time of 16(2) ms. Ground-state atoms in the cold gas are excited to high Rydberg states via resonant excitation through the intermediate $4s4p\,^1P_1$ and $4s4d\,^1D_2$ states. The MOT is operated at the center of an electrode stack, which serves to apply continuous and pulsed electric fields and field-ionize the Rydberg atoms for detection. We benchmark our MOT against previous implementations and find its performance consistent with state-of-the-art results in terms of temperature and trapping lifetime. Finally, we demonstrate Rydberg spectroscopy of calcium, confirming the system's suitability for ultracold Rydberg physics experiments.

I. INTRODUCTION

Magneto-optical traps (MOTs) have become an essential part of a large variety of experiments in atomic physics that require cold atoms for, e.g., high-precision spectroscopy[1], Bose-Einstein condensate[2], atomic clocks[3,4], quantum simulation[5], and the study of highly excited atoms[6] and molecules[7]. While many atomic species have already been laser cooled in a MOT[8–13], recent efforts have focused on alkaline-earth atoms. Because they possess two valence electrons, such atoms exhibit an energy-level structure that is both relatively simple compared to most atomic species, yet more complex than that of the widely used alkali atoms. This gives access to a broader range of physical phenomena and ways to control and manipulate the atoms. For example, the coupling between the spins of the two valence electrons, together with the Pauli exclusion principle, leads to the formation of singlet and triplet states. These states give rise to metastable excited levels that are crucial for metrological applications such as optical atomic clocks[14,15]. Additionally, the presence of narrow intercombination lines allows the atoms to reach much lower temperatures[16]. Finally, the presence of two electrons allows one to manipulate[17–20], directly laser cool[21,22], or interrogate[23] Rydberg atoms in a nondestructive manner.

The calcium atom is an advantageous candidate for exploring the applications in Rydberg physics given above, in particular because the autoionization rates of its doubly excited Rydberg states are low[24]. Ultracold Ca Rydberg gases have been much less explored than those of heavier species (Sr[22,23], Yb[4,17,19]), despite their energy level scheme being well suited for laser cooling and Rydberg excitation (see Fig. 1). The frequency of the primary cooling transition Ca($4s^2\,^1S_0 - 4s4p\,^1P_1$) lies in the visible range (423 nm), which is conveniently accessed with standard external cavity diode lasers, as used in our setup. Moreover, the broad linewidth of this transition (34 MHz) makes it ideal for scattering a large number of photons and cooling down the atoms efficiently. In addition ^{40}Ca, the most abundant isotope of Ca with 96.64(16)% abundance[25], has zero total nuclear spin, and hence no hyperfine structure, which further simplifies the cooling scheme.

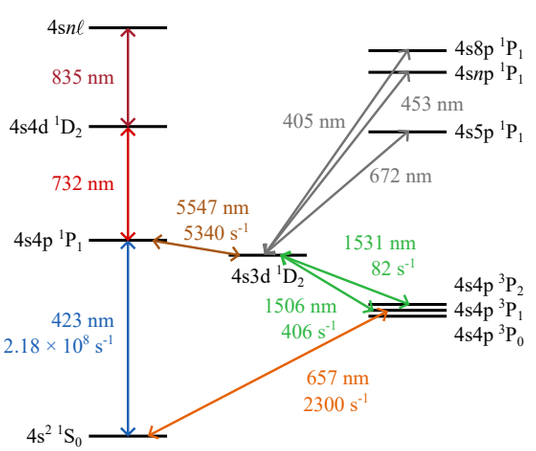

FIG. 1. Relevant energy levels and transitions of ^{40}Ca. Transition wavelengths were taken from Ref.[26]. Einstein A coefficients were taken from Ref.[27,28].

Calcium laser cooling was first reported in 1991, when one-dimensional optical molasses were used to deflect the

[a)] matthieu.genevriez@uclouvain.be

slow atoms coming out of a Zeeman slower[29]. A few years later, the first calcium MOT was demonstrated by the same group[1]. Since then, a number of Ca MOTs have been constructed[30–35], achieving typical number of atoms of $10^6 - 10^8$, and temperatures between 1.3 mK[1] and 9 mK[32]. The most pronounced differences among reported Ca MOTs lie in their trapping times, which span from 16 ms[34] to 2.5 s[35]. This large variability is primarily due to whether repumping systems are employed or not. The upper cooling state $4s4p\,^1P_1$ can leak through $4s3d\,^1D_2$ to the triplet states $^3P_2$ and $^3P_1$ (see Fig. 1), with a branching ratio of $1 : 10^5$ [36]. Although the ratio is sufficiently favourable for the atoms to be laser cooled, this decay pathway represents the main limiting factor to the MOT lifetime. Without any repumping, the trapping time is limited to ~ 16 ms[34]. Adding a 672 nm repump laser to drive the Ca($4s3d\,^1D_2 - 4s5p\,^1P_1$) transition increases the lifetime by a factor of three[34]. Further extension of the trapping time can be achieved either by choosing alternative repump wavelengths[27,35,37], or by adding a second repump laser[34]. Other parameters, such as beam size, available laser power, laser detuning, and optical alignment, can also influence the trapping time, number of trapped atoms, and/or final temperature[27,32,33].

In the last years, more advanced cooling schemes have been developed to bring the Ca MOT temperature well below its Doppler limit of 0.8 mK. One example is the two-color MOT[16,27,31], where the trap is first loaded using the broad 423-nm transition to capture a large number of atoms even with relatively large velocities, and a second, narrower-linewidth transition is used in a second stage to cool the atoms to lower temperatures.

The present paper reports the construction and characterization of a magneto-optical trap setup using the 423-nm laser cooling transition without any repumper. The magneto-optical trap is loaded with slow atoms coming out of a Zeeman slower, itself loaded with atoms from a Calcium oven. Each system is described in detail in Sec. II (II A-II E). The cold atoms in the MOT are then excited to high Rydberg states using the three-photon excitation scheme shown in Fig. 1. The scheme was used with thermal beams[38,39] but not in Ca MOTs, which focused on two-photon schemes[40]. The Rydberg atoms are then detected using a segmented electrode stack described in Sec. II F. The setup is characterized in Sec. III, with particular emphasis on the performances of the trap. We are finally discussing Rydberg excitation of the cold atomic cloud in the MOT, demonstrating the possibility of using the present setup to investigate ultracold gases of Ca Rydberg atoms.

II. EXPERIMENTAL SETUP

A. Overview of the experiment

Figure 2 presents a sectional view of the experimental setup 3D model. A single 423 nm external cavity diode laser (ECDL), frequency-locked to the Ca($4s^2\,^1S_0 - 4s4p\,^1P_1$) atomic transition, is employed for slowing, cooling, and trapping calcium atoms under ultra-high vacuum conditions ($< 10^{-8}$ mbar). The atoms are thermally emitted from a custom-built oven (Fig. 2**(1)**) operating at 500^{o}C, initially traveling at approximately 650 m/s. They are decelerated by a counter-propagating laser beam within a permanent-magnet Zeeman slower (Fig. 2**(2)**) to velocities below the capture velocity of the magneto-optical trap. The slowed atoms then enter the central region of the MOT chamber (Fig. 2**(3)**), where three orthogonal pairs of circularly polarized laser beams intersect. A pair of electromagnetic coils in anti-Helmholtz configuration on the top and bottom of the MOT chamber generates the required magnetic field gradient at the center of the trap. The cold atom cloud is observed via fluorescence using a CMOS camera and a photomultiplier tube.

B. Calcium oven

The oven was built based on the design presented in Ref.[41]. It consists of a cylindrical chamber with a 0.25-mm-diameter tantalum wire acting as the heating element, arranged around the lateral surface (Fig. 3). Calcium, in the form of small granules, is loaded into a cylindrical cartridge that is then inserted into the oven. The oven output is passing through capillary tubes with a radius of $R = 0.15$ mm and a length of $L = 15$ mm. The aspect ratio of the capillaries, L/R, determines the divergence of the atomic beam and, together with the temperature, the atomic flux. A resonant laser beam at 423 nm was shone perpendicularly to the atomic beam while scanning its frequency to measure the Doppler-broadened line profile. The Gaussian fitting of the line profile yielded a value for the half width at half maximum (HWHM) of 140 MHz. From the Doppler broadening, we inferred the transverse velocity spread (HWHM) of the atoms to be $\Delta v \simeq 60$ m/s, assuming a normal distribution. The divergence angle of the beam was then estimated using[41].

$$\theta = \frac{\Delta v}{v_{\rm beam}} \simeq 0.11\,\text{rad}\,, \tag{1}$$

with $v_{\rm beam}$ the most probable velocity of the atoms in the beam (545 m/s). It is larger than the divergence that would be expected for a single capillary with $L/R = 100$ in the long-channel limit, which is ~ 0.022 rad using the theoretical angular distribution given in Ref.[42]. This is most likely because of the imperfect alignment of the capillaries within the stack. The oven is mounted on a CF40 flange attached to the experiment's vacuum chamber and is surrounded by a thermal shield that reduces energy losses, enabling temperatures of approximately 500°C necessary to evaporate sufficient calcium atoms[43] with an input electrical power of 20 W. The atomic flux is

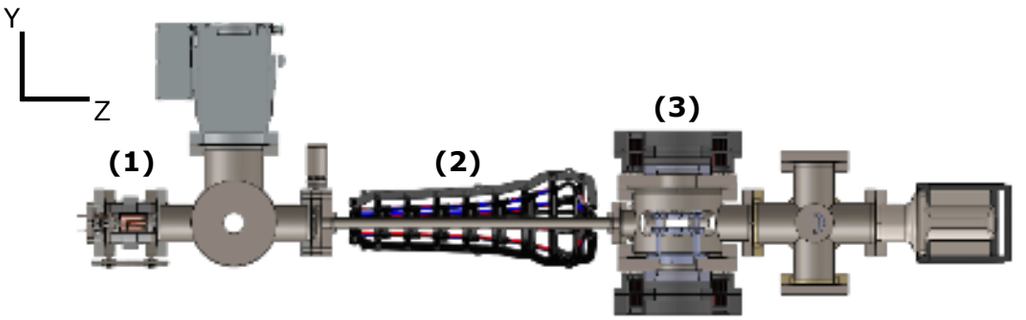

FIG. 2. Sectional view of the experimental setup, where **(1)** is the Ca oven, **(2)** is the permanent-magnet-based Zeeman slower, and **(3)** is the magneto-optical trap.

estimated, from the resonant absorption of 423-nm light, to be 10^{14} cm^{-2}s^{-1}.

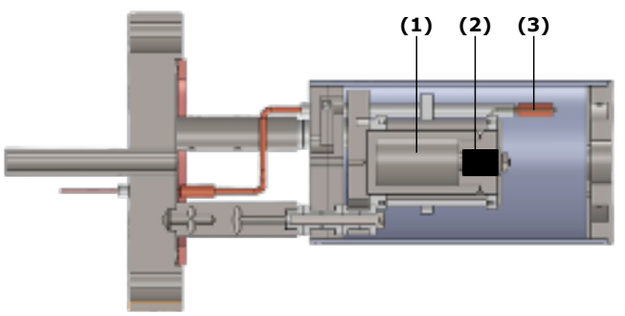

FIG. 3. Sectional view of the Ca oven. **(1)** is the cartridge where the Ca granules are loaded, **(2)** are the capillary tubes, and **(3)** is the tantalum wire.

C. Light production and control

Figure 4 shows a schematic view of the optical path. The Ca cooling and trapping is driven by a single external cavity diode laser (ECDL) at 423 nm[44], delivering a total optical power of 84 mW. This output is split into four optical paths, with the relative power in each path controlled by half-wave plates (HWPs) and polarizing beam splitters (PBSs).

The beam reflected from PBS1 is expanded with a Galilean telescope to a waist of 1.5 mm. This path (**1**) delivers 32 mW of optical power and serves as the Zeeman slowing beam.

The beam transmitted through PBS2 is sent through a 300-MHz acousto-optic modulator (AOM1). The first diffraction order is retroreflected in a cat's-eye configuration[45], resulting in a double pass through the modulator and a net frequency upshift of 600 MHz. This beam, sent into (**2**), carries 1 mW, and is used for frequency stabilization. The zeroth diffraction order from AOM1 constitutes beam (**3**), with 4 mW power, and is used for diagnostic purposes.

The beam reflected on PBS2 is directed to the acousto-optic modulator AOM2, also operated in a double-pass cat's-eye configuration with a tunable drive frequency. The resulting output (**4**) is upshifted by $600 + \Delta\nu_{\mathrm{MOT}}$ MHz, where $\Delta\nu_{\mathrm{MOT}} = -36$ MHz is the MOT detuning. This path (**4**) is provided with 8 mW of optical power. The beam is subsequently split into three paths to form the MOT beams, each expanded to 2 mm waist with a telescope.

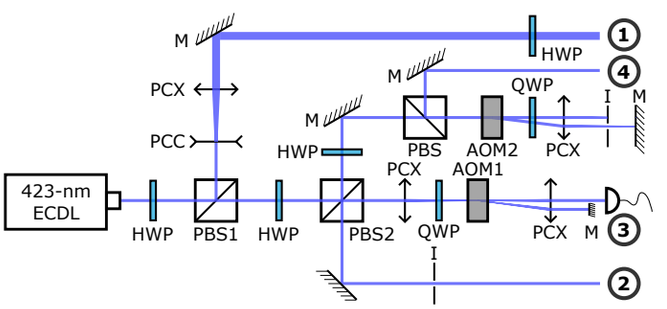

FIG. 4. Optical path schematics. **HWP**: half-wave plate. **QWP**: quarter-wave plate. **PBS**: polarizing beam splitter. **PCX**: plano-convex lens. **PCC**: plano-concave lens. **AOM**: acousto-optic modulator. **M**: mirror. **I**: iris. The optical paths $1-4$ correspond to the slowing beam, frequency stabilization, beam diagnosis, and MOT beam, respectively.

D. Zeeman slower

Zeeman slowers utilize the Zeeman effect to compensate for the decreasing Doppler shift as the atoms decelerate, maintaining resonance between the atoms and the slowing laser along the entire length of the slower. The ideal field profile along the atomic beam axis is given by[46]

$$B(z) = \frac{\eta\hbar k}{g_L \mu_B}\left[\sqrt{v_0^2 - \frac{\left(v_0^2 - v_f^2\right)}{L} z} - \frac{\delta}{k}\right], \qquad (2)$$

where η is a design parameter, k is the light wavenumber, μ_B is the Bohr magneton, $g_L = 1$ is the Landé factor of the upper state (the ground state is not Zeeman shifted), L is the Zeeman slower's length, δ is the laser detuning, and v_0 and v_f are the maximal velocity that can be slowed and the exit velocity, respectively.

Conventional Zeeman slowers often employ solenoidal coils to generate the required magnetic field profile[9]. Such systems require power supplies and water cooling due to the ohmic heating. To overcome that issue, we implemented a passive Zeeman slower based on permanent magnets[46].

In solenoid-based Zeeman slowers, the magnetic field is oriented along the direction of the atomic beam. Circularly polarized light (σ^+ or σ^-) is required to drive the transition between the ground-state magnetic sublevel $m = 0$ and the excited-state sublevels $m = \pm 1$. In contrast, in typical permanent-magnet designs, the magnetic field is oriented perpendicularly to the atomic beam. Driving the same transitions in this scheme is only possible with light linearly polarized perpendicular to the magnetic field. Since the magnetic sublevels $m = +1$ and $m = -1$ are equally coupled, only 50% of the total laser power is used to drive the right slowing transition.

Figure 5 shows the Zeeman slower 3D model. The design comprises nine segments, each containing eight NdFeB cuboid magnets. The first segment uses small magnets ($10 \times 3 \times 2$ mm)[47], and the rest use larger ones ($50 \times 6 \times 5$ mm)[48]. The magnets are radially arranged in Halbach configuration[49], which produces a homogeneous field in the transverse section (fig. 6**a**) while generating the required longitudinal profile (fig. 6**b**). A custom-made 3D-printed structure holds the magnets in position and ensures precise alignment of the slower with the atomic beam. The 3D-printed structure, fabricated from polylactic acid (PLA), can be printed within a day on regular printers, and it is sufficiently rigid to hold the magnets in place for over, at least, 2 years, which is the current time for which the slower has been operational. Moreover, the structure was designed such that magnet positioning is accurate to within 1 mm in the radial and longitudinal positions, and 0.5° in angle, ensuring that the actual configuration matches well the simulated one. With this design, the Zeeman slower can be assembled within a few hours and at a very small cost compared to solenoid-based designs. In this scheme, the atomic beam, magnetic field, and laser polarization are mutually orthogonal, as can be seen in fig. 6**a**.

The magnetic field, ranging from 800 G at the entrance of the slower to −250 G at the exit, along with the laser detuning ($\delta = -600$ MHz), allows the slowing of atoms moving at up to 720 m/s, corresponding to 64% of the thermal distribution at 500 °C. The magnetic field was measured experimentally twice, one year apart, yielding

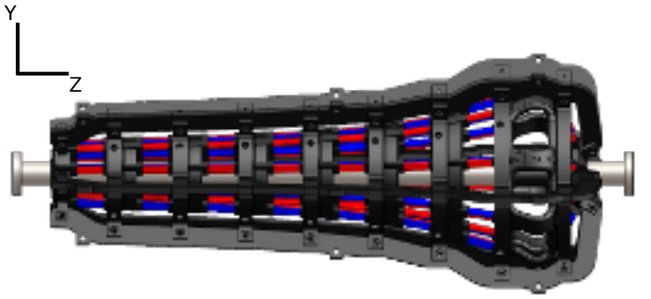

FIG. 5. Zeeman slower 3D model. The red and blue segments represent the north and south poles of the magnets, respectively. The black elements are the 3D-printed holding structure.

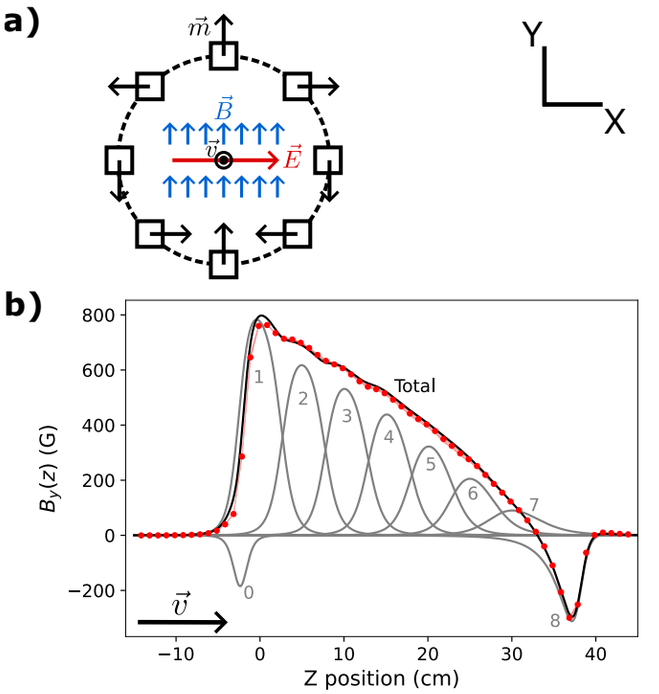

FIG. 6. **a)** Radial arrangement of the magnets in Halbach configuration. The black, blue, and red arrows represent the magnetic moment of the magnets $\vec{m}$, the homogeneous transverse magnetic field, and the laser polarization, respectively. **b)** Longitudinal magnetic field profile. The field was calculated from the field generated by each magnet using the formulas given in[46]. The contribution due to each segment of magnets is represented by gray solid lines, and the total field is represented by the black solid line. The red, filled circles and shaded area correspond to the experimental measurement of the magnetic field and its uncertainty, estimated as the standard deviation of three different measurements. The arrow in the bottom-left corner indicates the direction of propagation of the atomic beam.

the same results within a 2% error bar, without any adjustment of the 3D-printed structure (Fig. 6**b**, red solid circles).

The length of the Zeeman slower is set to ensure that the atoms are decelerated to a velocity of $\sim$ 35 m/s, without being completely stopped at its end. The acceleration considered to calculate the length of the slower is scaled by η so that $a = \eta \cdot a_{\max}$, where $\eta = 0.5$ and $a_{\max} = \Gamma\hbar k/2m$[46] is the maximal acceleration exerted by the light onto the atoms. Simulations of the trajectories of the atoms for different laser parameters indicated that a beam radius of 1.5 mm (at 32 mW total laser power) maximizes the number of atoms effectively slowed (Fig. 7). At low initial velocities ($v_0 < 60$ m/s), slowing in the final stages of the slower yields exit velocities below 35 m/s outside of the slower. The off-resonant radiation pressure of the 600-MHz red-detuned beam ($\sim$ 7% of the resonant force for the trajectories shown in Fig. 7), combined with the low velocity, is sufficient to further decelerate the atoms by a significant amount as they travel toward the MOT region. The fraction of atoms exiting the oven with such low velocities is however less than 0.1% of the total.

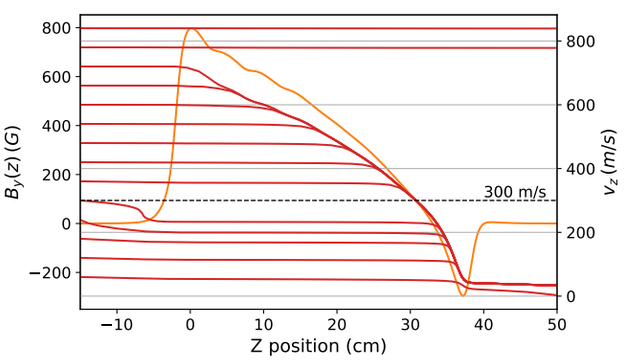

FIG. 7. Red lines: calculated trajectories of the atoms in the phase space of longitudinal position (z) and longitudinal velocity (v_z) as they travel across the Zeeman slower. Orange line: y component of the magnetic field on the axis of the Zeeman slower.

On the one hand, the present, permanent-magnet-based, passive design offers less flexibility than the solenoid-based counterpart, since it does not permit field adjustment via current tuning. Furthermore, only 50% of the laser power is effectively used for slowing the atoms. On the other hand, it eliminates any power consumption and thus, it avoids the necessity of any cooling system to prevent overheating. In addition, the simulation shows a rapid decay of the magnetic-field magnitude outside the Zeeman slower, reaching a value well below the Earth's magnetic field ($\sim$ 0.5 G) at the center of the MOT region located further downstream.

E. Magneto-optical trap

Magneto-optical traps combine Doppler cooling and the Zeeman effect to cool and trap neutral atoms[10]. They consist of three orthogonal pairs of counter-propagating laser beams with opposite circular polarizations intersecting at the center of a quadrupole magnetic field generated by two coils in anti-Helmholtz configuration.

In our setup, the center of the MOT is located approximately 12 cm downstream from the end of the Zeeman slower. We operate the MOT using a 423-nm laser red-detuned by −36 MHz from resonance. The beam is split into three using polarizing beam splitters and half-wave plates, which allow independent control of the power delivered to each arm. A quarter-wave plate is placed on each arm before entering the MOT chamber to convert the polarization of the beams from linear to circular. After the chamber, each beam is retroreflected using a mirror and an additional quarter-wave plate, which reverses the direction of the circular polarization and creates standing waves along all three spatial axes.

The quadrupole magnetic field required for confinement is generated by a pair of coils in a quasi-anti-Helmholtz configuration, positioned above and below the MOT chamber. The coils were custom-built in-house from a copper ribbon (20 mm wide, 0.7 mm thick). Each coil consists of two vertically stacked spirals with 15 turns each, having internal and external diameters of 118 mm and 168 mm, respectively (Fig. 8). The turns are spaced by 0.5 mm with pieces of electric tape, and the two spirals are separated by 10 mm. With a current of 150 A (6 V), the coils produce a magnetic field gradient of 30(1) G/cm along the axial direction and 15.3(3) G/cm in the radial directions. The magnetic field experimentally measured along both the radial and the axial directions of the coils falls in very good agreement with the prediction built from the theoretical field of circular current loops[50], as shown in Fig. 9

To dissipate the heat produced by the high current circulating in the copper ribbon ($\sim$ 1 kW), the coils were enclosed in custom-designed, watertight housings fabricated in-house from polyvinyl chloride (PVC) (see Fig. 8). Deionized water circulates in the 0.5-mm spacing between the coil windings, which is left free apart from a few spacing elements, ensuring an efficient heat dissipation due to the large contact area between water and copper, thanks to the ribbon shape of the conductor. These housings are connected in parallel via 6 mm diameter water pipes to a water chiller, which continuously circulates the deionized water through them to maintain the temperature at 25°C. The present design does not require hollow conductors in which water is passed through a hole in the center of the wire. The conductance of the cooling system is large, such that the pressure drop across the coils is small, and water chillers with relatively small pumps can be used. The simplicity of the setup means it can be wound manually, which makes it attractive for coils that require a small number of windings, and its high

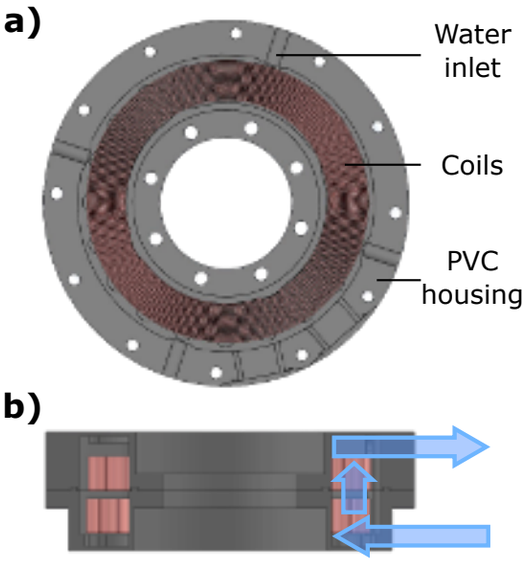

FIG. 8. Top-view **(a)** and cut-half side-view **(b)** of the MOT coils. The blue arrows on **(b)** represent the water flow for cooling the coils.

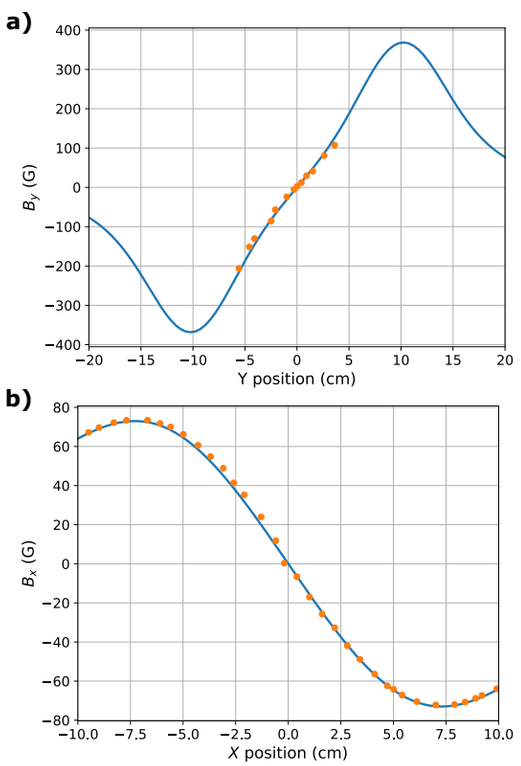

FIG. 9. Magnetic field along the axial **a)** and radial **b)** directions of the coils for a current of 150 A. The blue line represents the calculated field, and the orange solid circles, the experimental measurements.

heat dissipation capabilities mean the coils can be operated at large currents. We have operated on a regular basis the coils up to 220 A, the limit of our power supply, while being able to keep the water flow at a constant temperature of 25°C.

To ensure that the MOT laser beams cross at the position where the magnetic field is zero, we used the directional Hanle effect following the approach detailed in Ref.[51]. One of the horizontal MOT beams was converted to linear polarization and scanned both horizontally and vertically across the MOT region while being kept on resonance with the $4s^2\,{}^1S_0 - 4s4p\,{}^1P_1$ transition. Its linear polarization was set parallel to the imaging camera, such that in the absence of any magnetic field, only a negligible amount of fluorescence light was emitted in the direction of the camera because of the $\sin^2(\theta)$ emission diagram of the $J = 1, M_J = 0 \rightarrow J = 0, M_J = 0$ fluorescing transition. When the magnetic field gradient of the MOT is switched on, the nonzero magnetic field washes out this effect, and fluorescent light is detected by the camera, with the exception of the region where the magnetic field is zero, which then appears as a dark spot in the image, as shown in Fig. 10. This allows to easily locate the zero-magnetic-field region in the vacuum chamber and to align the MOT beams accordingly.

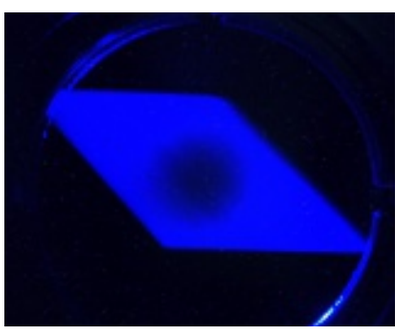

FIG. 10. Zero magnetic field position (dark area) inside the MOT observed by using the directional Hanle effect. The image was generated by combining the frames of a video recorded while sweeping a 423-nm laser across the MOT region, and subsequently editing it to visualize only the brightest pixels, which gives the laser beam the rhombus-like shape observed in the picture. The edges of the 63-CF laser window placed on top of the MOT chamber are also visible.

The experimental parameters used to operate the MOT are summarized in Table I.

F. Electrode stack

To apply electric fields of arbitrary direction in the MOT region, we designed and constructed an electrode-stack assembly consisting of two split rings made of stainless steel 316 with internal and external diameters of 20 and 40 mm, respectively. A schematic of the electrodes is presented in Fig. 11**a**. The rings, vertically stacked with 16 mm separation, are each segmented into four indepen-

Oven temperature	723 K	**Pressure in the MOT chamber**	10^{-9} mbar
MOT detuning	−36 MHz	**Zeeman detuning**	−600 MHz
MOT power in each arm	2.13, 2.30, 0.687 mW	**Zeeman power**	32 mW
MOT waist	2 mm	**Zeeman waist**	1.5 mm
Saturation parameter in each MOT arm	2.09, 2.25, 0.67	**Saturation parameter Zeeman**	15
$\nabla \vec{B}_{\mathrm{MOT}}$ **axial**	30 G cm^{-1}	$\nabla \vec{B}_{\mathrm{MOT}}$ **radial**	15 G cm^{-1}

TABLE I. MOT and Zeeman slower operation parameters.

dently addressable electrodes, allowing precise control of the electric-field orientation according to experimental requirements.

The electrodes generate electric fields that enable the pulsed-field ionization[52] of Rydberg atoms and the guiding of the resulting ions toward a channel electron multiplier (CEM, also called channeltron) for their detection. Pulsed voltages of up to 3 kV can be applied to the electrodes, which allows the field ionization of Rydberg states down to $n \sim 26$. Figure 11**b** shows a simulation of ion trajectories when voltages of +2 kV are applied on the four electrodes opposite to the CEM (1, 2, 5, 6), corresponding to an electric field magnitude of 559 V cm^{-1} in the MOT region. All ions are efficiently steered onto the CEM.

A further application of the electrodes is the compensation of stray electric fields within the MOT region, since the polarizability of the Rydberg atoms, scaling as n^7 [52], makes them extremely sensitive to even weak residual fields. The segmentation of the electrodes means that stray fields can be compensated in all three directions of space.

Finally, the electric fields generated by the electrodes may also be used for coupling the different states within a Stark manifold, enabling the excitation of high-ℓ Rydberg states via the Stark switching technique[53].

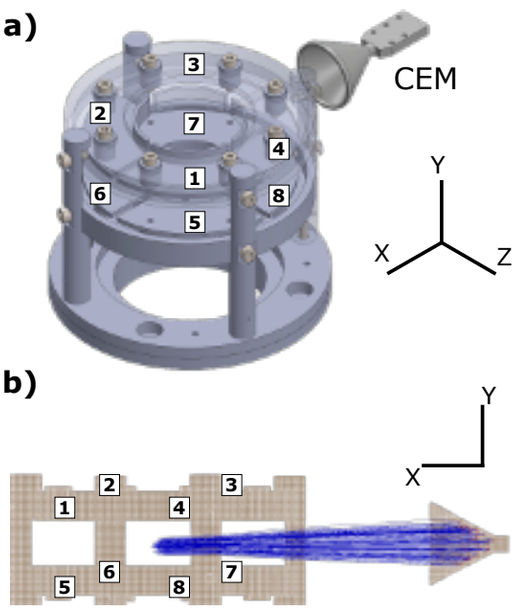

FIG. 11. **a)** 3D model of the electrode stack and the CEM. Each electrode is numbered from 1 to 8. The electrodes 1, 2, 5, and 6 generate the extraction field that directs the ions toward the CEM. **b)** Simulation on SIMION[54] of the trajectories of the ions generated inside the MOT when applying an extraction field to steer them into the CEM.

III. RESULTS

The velocity distribution of the atoms was measured after the Zeeman slower, both with and without the slowing laser, by shining a second 423-nm probe laser in the MOT region at a $\sim 45°$ angle with respect to the atomic beam. The intensity of the atomic fluorescence, recorded with a photomultiplier tube (PMT) while scanning the probe-laser frequency, is presented in Fig. 12.

When the slowing laser beam is switched on, the atomic velocity distribution is modified in two ways. First, a sharp peak around 35 m/s demonstrates the Zeeman slowing. The maximum entrance velocity at which the atoms are slowed is 720 m/s, in accordance with the simulated trajectories shown in Fig. 7. The final velocity of the atoms is in good agreement with the design and calculated exit velocities, and well below the capture velocity of the MOT of ~ 60 m/s.

The slowing-beam diameter ($2w_0 = 3$ mm) is significantly smaller than the diameter of the Zeeman-slower vacuum tube (15 mm). The atomic-beam divergence and transverse-velocity spread are much larger than the geometrical acceptance of the Zeeman slower tube, therefore the atomic-beam size in the MOT chamber is geometrically limited by the Zeeman-slower vacuum tube. The probe laser beam intersects the atoms regardless of their velocity along its line of sight (beam waist $\sim$ 1 mm). Because its waist size is smaller than the radius of the

atomic beam in the MOT chamber, it does not intersect with all atoms within a section of the atomic beam, but only with those along its line of sight. The relative fraction of slowed atoms, obtained by integrating the area of the Zeeman peak and comparing it to the total area of the velocity distribution below the cut-off velocity, is approximately 20%, in agreement with the ratio between the slowing-laser and atomic-beam radii, which is also 20%. The fact that not all observed atoms are slowed can then be explained by the geometrical overlap between the laser beam and the atomic beam, A larger fraction of atoms could be slowed by increasing the laser beam diameter and its power accordingly.

Second, a depletion around 250 m/s is observed, accompanied by a redistribution of the population toward adjacent lower velocities. This indicates that the atoms initially on resonance with the slowing beam are partially slowed before entering the Zeeman slower until they eventually fall out of resonance, which is consistent with a slowing process without magnetic compensation. This effect arises because the sizes of the oven output and the slowing beam are comparable; therefore, all atoms emerging from the oven at that velocity are slightly slowed before reaching the Zeeman slower. However, due to the transverse velocity spread and the resulting size mismatch between the atomic and slowing beams along the Zeeman slower, only a fraction of these atoms remain within the slowing beam and are decelerated to the final velocity of 35 m/s (see Fig. 7, trajectories between 200 and 300 m/s). The remaining atoms leave the slowing beam and continue propagating along the Zeeman slower without further deceleration.

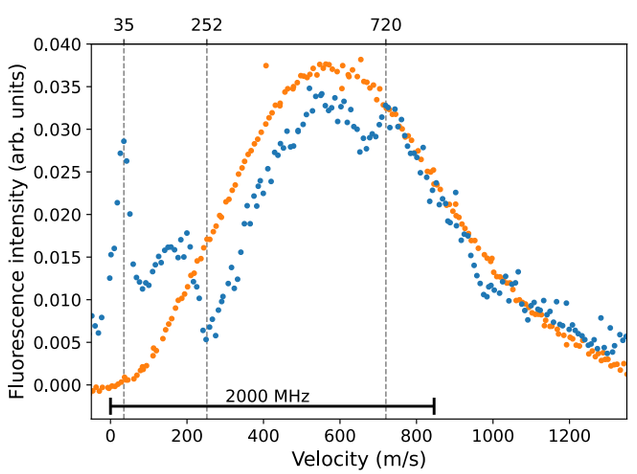

FIG. 12. Velocity distribution of the atoms measured after the Zeeman slower without the slowing beam (orange full circles), and with the slowing beam (blue full circles).

The slow atoms exiting the Zeeman slower are then captured in the MOT. The atomic cloud size, the MOT trapping time, and the number and density of trapped atoms were determined by monitoring the 423-nm fluorescence of the cold atoms with both CMOS cameras and a PMT. A typical fluorescence image of the MOT is shown in Fig. 13. The fluorescence intensity distribution closely resembles a Gaussian distribution, and the MOT size defined as the full width at half maximum (FWHM) of the Gaussian fit to the measured intensity profile, is 0.83(1) mm and 1.90(3) mm along the X and Y axes, respectively. The elongated shape in the vertical direction, rather than a spherical distribution, arises from the lower optical power in the corresponding vertical MOT beams (see Table I).

To determine the number of trapped atoms, the optical power of the fluorescence light emitted through the solid angle defined by the surface of the imaging viewport was measured using a calibrated, high-sensitivity photodiode. From the measured power of 4 nW, we estimate the atom number to be approximately 10^6, corresponding to a density of 10^8 cm^{-3}. This value represents a lower bound to the real atom number since the atoms in the metastable $4s3d\,^1D_2$ and $4s4p\,^3P_1$ do not fluoresce rapidly nor at the 423-nm wavelength of our detection system, and therefore did not contribute to the measured signal.

Previous studies have shown that adding lasers at 672 or 405 nm increases the number of trapped atoms inside the MOT by a factor of approximately 13 [34] and 20 [27], respectively. These wavelengths repump the population from the $4s3d\,^1D_2$ state to the $4s5p\,^1P_1$ and the $4s8p\,^1P_1$ states, respectively, thereby preventing decay into the long-lived $4s4p\,^3P_2$ metastable state, which, with a lifetime of 118 min[55], constitutes the main loss channel of the MOT. Such repumpers not only increase the number of atoms but also extend the MOT trapping time, by a factor of three to nearly six in the case of the 672-nm laser, as reported in[34,35]. Alternative repump schemes have also been investigated in Ref.[35], identifying 453 nm as the optimal wavelength for maximizing both the number of trapped atoms and the trapping time, with values up to 2.5 s reported. Experimental realization of the 453 nm repump scheme was carried out in Ref.[37], where the MOT lifetime for even calcium isotopes was extended from 20 ms to 1.9 s. The implementation of any of these repump schemes in future iterations of the experiment is considered.

The temperature of the Ca atoms in the MOT was determined from the ballistic expansion of the atomic cloud. First, the MOT was loaded for 140 ms. The MOT beams were then switched off for a certain delay time, after which an image of the atomic cloud was acquired using the side-view camera with a given exposure time t_{exp}. The camera was synchronized with the reactivation of the MOT beams in order to illuminate the cloud. However, reactivating the MOT beams induces partial recompression of the cloud, the extent of which depends on the duration for which the beams are switched on, and therefore, on the camera exposure time. As a result, longer exposure times lead to increased recompression and a smaller observed cloud size. To track the expansion of the cloud over time, the MOT was reloaded for

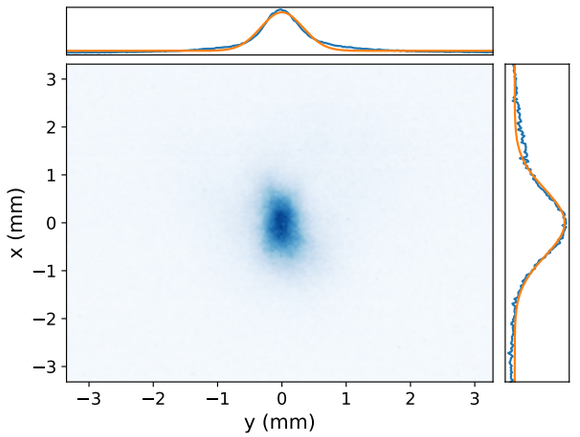

FIG. 13. False-color fluorescence image of the MOT captured with the side-view camera, showing the signal projections integrated along the X and Y axes (blue solid lines) and the Gaussian fitting curves (orange solid lines).

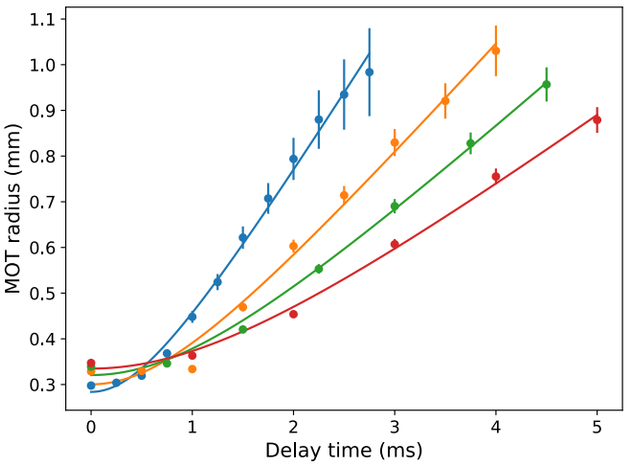

FIG. 14. Ballistic expansion of the MOT cloud (solid circles) and fits to Eq. 3 (solid lines). The data recorded at 0.25, 0.5, 0.75, and 1 ms exposure time is represented in blue, orange, green, and red, respectively.

each measurement, with the images acquired at progressively longer delay times while keeping the exposure time fixed. The experiment was repeated four times using four different camera exposure times: 0.25 ms (blue solid circles), 0.5 ms (orange solid circles), 0.75 ms (green solid circles), and 1 ms (red solid circles).

The experimental data were fit to an equation describing the increase of the RMS radius of the atomic cloud r throughout the duration of the ballistic expansion t (see e.g. Ref.[56]). To account for the recompression, an additional factor was added to the $k_B T t^2/m$ term to account for the overdamped motion of the atoms when the MOT beams are switched back on during the exposure time t_{exp} necessary to acquire the image. The formula is then

$$r(t) = \sqrt{r_0^2 + \frac{k_B T}{m} t^2 e^{-(\frac{t_{exp}}{\tau_d})^2}}\,, \tag{3}$$

where r_0 denotes the initial radius of the atomic cloud, defined as the standard deviation of the spatial fluorescence distribution before ballistic expansion; k_B is the Boltzmann constant; T is the MOT temperature; m is the mass of ^{40}Ca; t is the delay time between switching off the MOT and triggering the camera; t_{exp} is the camera exposure time; and τ_d is the characteristic damping time of the MOT. The latter was calculating using $\tau_d = 2\Gamma_{\rm MOT}/\omega_{\rm MOT}^2$, with $\Gamma_{\rm MOT}$ the MOT damping rate (~ 43 kHz in the present case) and $\omega_{\rm MOT}$ the MOT trapping frequency (~ 7 kHz). Both can be calculated from standard formulas[57] using the experimental parameters we measured and listed in table I.

The temperature obtained from fitting the different data sets is 1.0(3) mK, in agreement with the value reported in[27] and consistent with the Doppler limit of 0.8 mK. Small variations in the initial MOT radius, r_0, of about 50 μm can be observed. The fits were repeated after averaging and fixing the value of r_0, leaving only the temperature as a free parameter, and yielded the same result, demonstrating that these small fluctuations represent drifts of the MOT cloud size over long periods of time, and not fluctuations of the temperature.

Finally, the loading time of the MOT was measured by rapidly switching on the MOT laser beams with an acousto-optic modulator and monitoring the increase of fluorescence in time with the PMT. With a constant flux of atoms arriving in the MOT chamber from the Zeeman slower, turning on the MOT laser beams causes the slow atoms entering the trapping region to be cooled and confined. As a result, the MOT fluorescence increases as the atomic density grows. The evolution of the population trapped in the MOT over time is given by[58]

$$\frac{{\rm d}N}{{\rm d}t} = R - \gamma N(t) - \beta \bar{n} N\,, \tag{4}$$

where R is the loading rate of the MOT, $\gamma = \gamma_{\rm col} + \gamma_{\rm met}$ is the rate of one-atom loss events, which includes collisions with the background gas ($\gamma_{\rm col}$) and decay to metastable states ($\gamma_{\rm met}$). N denotes the atom number, β is the two-body loss rate corresponding to inelastic collisions between trapped atoms, and $\bar{n}$ is the average atomic density within the MOT.

At relatively low optical power and atomic density, typically $\gamma \gg \beta\bar{n}$ and the evolution of the number of atoms N when loading the MOT is

$$N(t) = N_\infty(1 - \exp -t/\tau)\,, \tag{5}$$

with $N_\infty \simeq 10^6$ and τ being the loading time of the MOT. In the low-power, low-density limit, the loading time and trapping (decay) times are identical.

Figure 15 shows the difference between the steady state fluorescence signal ($\propto N_\infty$) and the fluorescence signal at different times after switching on the MOT beams ($\propto N(t)$). A fit to the function $Ae^{-t/\tau}$ yields a loading time of 16(2) ms. This value is consistent with previous reports for calcium MOTs operated under similar conditions without a repumping system[32,34], and it corresponds to the limit set by the decay into the metastable state $4s4p\,^3P_2$.

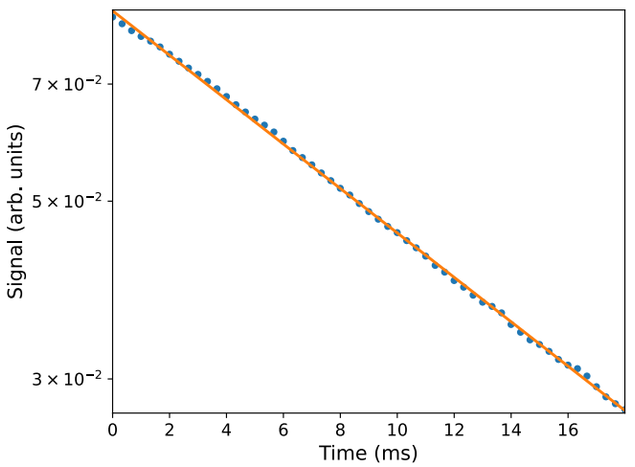

FIG. 15. Difference between the MOT steady-state fluorescence and the MOT fluorescence at a given time during loading on a logarithmic scale. The solid circles represent the experimental measurements, and the solid line, the exponential fitting yielding a trapping time of 16(2) ms.

The ground-state Ca atoms in the MOT can then be excited to high Rydberg states by means of resonant three-photon excitation. The first transition ($4s^2\,^1S_0$ – $4s4p\,^1P_1$) is driven by the MOT beams. The second ($4s4p\,^1P_1$ - $4s4d\,^1D_2$, 732 nm) and third transitions ($4s4d\,^1D_2$ - $4snp\,^1P_1$ or $4snf\,^1F_3$, 835 nm) are driven by commercial external-cavity diode lasers whose frequencies are stabilized to an accurate wavemeter. Figure 16 shows a typical excitation spectrum to the $4s54p\,^1P_1$ Rydberg level, recorded after letting the second and third lasers interact with the atoms in the MOT for ~ 100 μs. An electric field of 2 kV is then applied with a fast high-voltage switch to the four electrodes on the side opposite to the CEM. The electric field ionizes the Rydberg atoms and accelerates the Ca^+ onto the CEM, where they are detected and counted with fast electronics. With this setup, we have recorded $4snp$ and $4snf$ Rydberg states from $n \sim 26$ up to $n > 150$, at excitation frequencies in excellent agreement with Ref.[38].

IV. CONCLUSIONS

We have presented an experimental apparatus for laser cooling and trapping Ca atoms in an ultra-high-vacuum

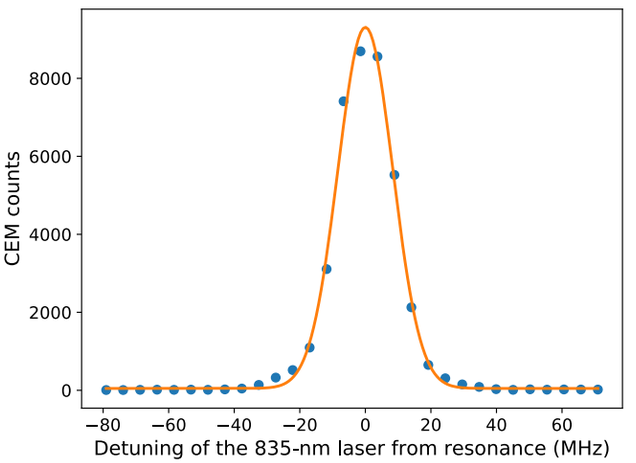

FIG. 16. Rydberg spectrum obtained by pulsed-field ionization of the $4s54p,\,^1P_1$ Rydberg state while scanning the 835-nm laser frequency. The blue solid circles and the orange line correspond to the experimental values and the Gaussian fitting, respectively.

environment using the Ca($4s^2,^1S_0 - 4s4p,^1P_1$) transition at 423 nm. Ground-state atoms are then excited to high Rydberg states with a three-photon resonant-excitation scheme, and an electrode-stack system surrounding the trapping volume enables the application of electric fields, the field ionization of the Rydberg atoms, and the detection of the resulting positive ions. In the first stage of the experiment, the Ca atoms are evaporated in an oven, and emitted in a beam with 0.11 rad divergence at a most probable velocity of 650 m/s. The atoms are then slowed down to a velocity of 35 m/s by means of a permanent-magnet-based Zeeman slower. Subsequently, the slow atoms are captured in a magneto-optical trap, where they remain confined for 16 ms on average, while they lose energy until reaching temperatures around 1 mK with a density of approximately 10^8 cm^{-3}. These results are consistent with previous reports of magneto-optical traps of similar characteristics[27,32,34]. Once the atoms are cooled and trapped in the MOT, the electrode stack can be used to apply electric fields to, e.g., control Rydberg excitation via Stark switching, as well as for pulsed-field ionization and detection of the Rydberg states. The results discussed above confirm that the setup described in the present paper provides a robust platform for experiments with ultracold Ca Rydberg atoms. As a next step, this setup will be used to perform high-resolution spectroscopy of the Rydberg Stark states of Ca. Following excitation of the atoms to Rydberg states, the ion-core transition $[4s_{1/2}]n\ell - [4p_{1/2,3/2}]n\ell$ will be driven to produce doubly excited Rydberg states. This will enable a direct investigation of the autoionization rates predicted in Ref.[24]. Finally, we aim to experimentally implement the scheme proposed in Ref.[21] for the direct laser cooling of Rydberg atoms.

V. ACKNOWLEDGMENTS

This work was supported by the Fonds de la Recherche Scientifique—FNRS under MIS Grant No. F.4027.24 and IISN Grant No. 4.4504.10, and by the Secuweb project (0100085) of the Interreg France-Wallonia-Flanders programme, an initiative co-financed by the European Union (European Regional Development Fund).

E.M.B. is financially supported by a FRIA fellowship from the Fonds de la Recherche Scientifique – FNRS.

X.U. is a Senior Research Associate of the Fonds de la Recherche Scientifique – FNRS

The authors are grateful to R. P. de Groote and Á. Koszorús for lending the 423-nm probe laser.

[1] Th. Kisters, K. Zeiske, F. Riehle, and J. Helmcke, "High-resolution spectroscopy with laser-cooled and trapped calcium atoms," Appl. Phys. B **59**, 89–98 (1994).
[2] M. H. Anderson, J. R. Ensher, M. R. Matthews, C. E. Wieman, and E. A. Cornell, "Observation of Bose-Einstein Condensation in a Dilute Atomic Vapor," Science **269**, 198–201 (1995).
[3] H. Wang and G. Iyanu, "MOT-based continuous cold Cs-beam atomic clock," in *2010 IEEE International Frequency Control Symposium* (2010) pp. 454–458.
[4] N. Hinkley, J. A. Sherman, N. B. Phillips, M. Schioppo, N. D. Lemke, K. Beloy, M. Pizzocaro, C. W. Oates, and A. D. Ludlow, "An Atomic Clock with 10–18 Instability," Science **341**, 1215–1218 (2013).
[5] H. Labuhn, D. Barredo, S. Ravets, S. de Léséleuc, T. Macrì, T. Lahaye, and A. Browaeys, "Tunable two-dimensional arrays of single Rydberg atoms for realizing quantum Ising models," Nature **534**, 667–670 (2016).
[6] W. Li, I. Mourachko, M. W. Noel, and T. F. Gallagher, "Millimeter-wave spectroscopy of cold Rb Rydberg atoms in a magneto-optical trap: Quantum defects of the ns, np, and nd series," Phys. Rev. A **67**, 052502 (2003).
[7] A. L. Collopy, S. Ding, Y. Wu, I. A. Finneran, L. Anderegg, B. L. Augenbraun, J. M. Doyle, and J. Ye, "3D Magneto-Optical Trap of Yttrium Monoxide," Phys. Rev. Lett. **121**, 213201 (2018).
[8] D. J. Wineland, R. E. Drullinger, and F. L. Walls, "Radiation-Pressure Cooling of Bound Resonant Absorbers," Phys. Rev. Lett. **40**, 1639–1642 (1978).
[9] W. D. Phillips and H. Metcalf, "Laser Deceleration of an Atomic Beam," Phys. Rev. Lett. **48**, 596–599 (1982).
[10] E. L. Raab, M. Prentiss, A. Cable, S. Chu, and D. E. Pritchard, "Trapping of Neutral Sodium Atoms with Radiation Pressure," Phys. Rev. Lett. **59**, 2631–2634 (1987).
[11] E. S. Shuman, J. F. Barry, and D. DeMille, "Laser cooling of a diatomic molecule," Nature **467**, 820–823 (2010).
[12] L. Baum, N. B. Vilas, C. Hallas, B. L. Augenbraun, S. Raval, D. Mitra, and J. M. Doyle, "1D Magneto-Optical Trap of Polyatomic Molecules," Phys. Rev. Lett. **124**, 133201 (2020).
[13] N. B. Vilas, C. Hallas, L. Anderegg, P. Robichaud, A. Winnicki, D. Mitra, and J. M. Doyle, "Magneto-optical trapping and sub-Doppler cooling of a polyatomic molecule," Nature **606**, 70–74 (2022).
[14] Th. Udem, S. A. Diddams, K. R. Vogel, C. W. Oates, E. A. Curtis, W. D. Lee, W. M. Itano, R. E. Drullinger, J. C. Bergquist, and L. Hollberg, "Absolute Frequency Measurements of the Hg^+ and Ca Optical Clock Transitions with a Femtosecond Laser," Phys. Rev. Lett. **86**, 4996–4999 (2001).
[15] M. Yin, Q. Xu, Y. Wang, J. Ren, Y. Guo, and H. Chang, "Development of the strontium optical lattice clock at national time service center," in *2018 European Frequency and Time Forum (EFTF)* (2018) pp. 374–376.
[16] C. Degenhardt, H. Stoehr, C. Lisdat, G. Wilpers, H. Schnatz, B. Lipphardt, T. Nazarova, P.-E. Pottie, U. Sterr, J. Helmcke, and F. Riehle, "Calcium Optical Frequency Standard with Ultracold Atoms: Approaching 10^{-15} Relative Uncertainty," Phys. Rev. A **72**, 062111 (2005).
[17] J. T. Wilson, S. Saskin, Y. Meng, S. Ma, R. Dilip, A. P. Burgers, and J. D. Thompson, "Trapping Alkaline Earth Rydberg Atoms Optical Tweezer Arrays," Phys. Rev. Lett. **128**, 033201 (2022).
[18] A. P. Burgers, S. Ma, S. Saskin, J. Wilson, M. A. Alarcón, C. H. Greene, and J. D. Thompson, "Controlling Rydberg Excitations Using Ion-Core Transitions in Alkaline-Earth Atom-Tweezer Arrays," PRX Quantum **3**, 020326 (2022).
[19] K.-L. Pham, T. F. Gallagher, P. Pillet, S. Lepoutre, and P. Cheinet, "Coherent Light Shift on Alkaline-Earth Rydberg Atoms from Isolated Core Excitation without Autoionization," PRX Quantum **3**, 020327 (2022).
[20] M. Wirth, C. Hölzl, A. Götzelmann, E. Pultinevicius, and F. Meinert, "Quadrupole Coupling of Circular Rydberg Qubits to Inner Shell Excitations," Phys. Rev. Lett. **133**, 123403 (2024).
[21] A. Bouillon, E. Marin-Bujedo, and M. Génévriez, "Direct Laser Cooling of Rydberg Atoms with an Isolated-Core Transition," Phys. Rev. Lett. **132**, 193402 (2024).
[22] L. Lachaud, B. Muraz, A. Couto, J.-M. Raimond, M. Brune, and S. Gleyzes, "Slowing Down a Coherent Superposition of Circular Rydberg States of Strontium," Phys. Rev. Lett. **133**, 123202 (2024).
[23] A. Muni, L. Lachaud, A. Couto, M. Poirier, R. C. Teixeira, J.-M. Raimond, M. Brune, and S. Gleyzes, "Optical coherent manipulation of alkaline-earth circular Rydberg states," Nat. Phys. **18**, 502–505 (2022).
[24] E. Marin-Bujedo and M. Génévriez, "Autoionization of high-l core-excited Rydberg states of alkaline-earth-metal atoms," Phys. Rev. A **108**, 012816 (2023).
[25] E. J. Salumbides, V. Maslinskas, I. M. Dildar, A. L. Wolf, E.-J. Van Duijn, K. S. E. Eikema, and W. Ubachs, "High-precision frequency measurement of the 423-nm Ca i line," Phys. Rev. A **83**, 012502 (2011).
[26] "Atomic Spectra Database," NIST (2009).
[27] W. Adamczyk, S. Koch, C. Politi, H. F. Passagem, C. Fischer, P. Filippov, F. Berterottière, D. Kienzler, and J. Home, "Two-photon cooling of calcium atoms," Phys. Rev. A **111**, 043101 (2025).
[28] G. Wilpers, C. W. Oates, S. A. Diddams, A. Bartels, T. M. Fortier, W. H. Oskay, J. C. Bergquist, S. R. Jefferts, T. P. Heavner, T. E. Parker, and L. Hollberg, "Absolute frequency measurement of the neutral^{40} Ca optical frequency standard at 657 nm based on microkelvin atoms," Metrologia **44**, 146–151 (2007).
[29] A. Witte, T. Kisters, F. Riehle, and J. Helmcke, "Laser cooling and deflection of a calcium atomic beam," J. Opt. Soc. Am. B, JOSAB **9**, 1030–1037 (1992).
[30] T. Kurosu and F. Shimizu, "Laser Cooling and Trapping of Calcium and Strontium," Jpn. J. Appl. Phys. **29**, L2127 (1990).
[31] J. Grünert and A. Hemmerich, "Sub-Doppler magneto-optical trap for calcium," Phys. Rev. A **65**, 041401 (2002).
[32] R. L. Cavasso Filho, D. A. Manoel, D. R. Ortega, A. Scalabrin, D. Pereira, and F. C. Cruz, "Calcium magneto-optical trap loaded from a decelerated atomic beam," Braz. J. Phys. **33**, 355–362 (2003).
[33] U. Dammalapati, I. Norris, L. Maguire, M. Borkowski, and E. Riis, "A compact magneto-optical trap apparatus for calcium," Meas. Sci. Technol. **20**, 095303 (2009).
[34] C. Burrows, *Repump Methods for Magneto-Optically Trapped Calcium Atoms*, Ph.D. thesis, University of Strathclyde (2012).
[35] M. Mills, P. Puri, Y. Yu, A. Derevianko, C. Schneider, and E. R. Hudson, "Efficient repumping of a Ca magneto-optical trap," Phys. Rev. A **96**, 033402 (2017).
[36] N. Beverini, F. Giammanco, E. Maccioni, F. Strumia, and G. Vissani, "Measurement of the calcium $^1P_1$–$^1D_2$ transition rate in a laser-cooled atomic beam," J. Opt. Soc. Am. B, JOSAB **6**, 2188–2193 (1989).
[37] T.-Y. Xia, W.-W. Sun, S. Ebser, W. Jiang, G.-M. Yang, H.-

M. Zhu, Y.-C. Fu, F. Huang, G.-D. Ming, T. Xia, and Z.-T. Lu, "Atom-Trap Trace Analysis of ^{41}Ca/Ca down to the 10^{-17} Level," Nat. Phys. **19**, 904–908 (2023).

[38] M. Miyabe, C. Geppert, M. Kato, M. Oba, I. Wakaida, K. Watanabe, and K. D. A. Wendt, "Determination of Ionization Potential of Calcium by High-Resolution Resonance Ionization Spectroscopy," J. Phys. Soc. Jpn. **75**, 034302 (2006).

[39] W. Nörtershäuser, B. A. Bushaw, P. Müller, and K. Wendt, "Line shapes in triple-resonance ionization spectroscopy," Appl. Opt., AO **39**, 5590–5600 (2000).

[40] B. B. Zelener, S. A. Saakyan, V. A. Sautenkov, E. V. Vilshanskaya, B. V. Zelener, and V. E. Fortov, "Measurements of the Rydberg Transition Energies for the $n\,^1S_0$ State and the Ionization Potential for ^{40}Ca Atoms," Jetp Lett. **110**, 761–765 (2019).

[41] M. Schioppo, N. Poli, M. Prevedelli, St. Falke, Ch. Lisdat, U. Sterr, and G. M. Tino, "A compact and efficient strontium oven for laser-cooling experiments," Rev. Sci. Instrum. **83**, 103101 (2012).

[42] H. C. W. Beijerinck and N. F. Verster, "Velocity distribution and angular distribution of molecular beams from multichannel arrays," J. Appl. Phys. **46**, 2083–2091 (1975).

[43] I. Norris, *Laser Cooling and Trapping of Neutral Calcium Atoms*, Ph.D. thesis, University of Strathclyde (2009).

[44] MOGLABS LDL Littrow enhanced ECDL.

[45] E. A. Donley, T. P. Heavner, F. Levi, M. O. Tataw, and S. R. Jefferts, "Double-pass acousto-optic modulator system," Review of Scientific Instruments **76**, 063112 (2005).

[46] P. Cheiney, O. Carraz, D. Bartoszek-Bober, S. Faure, F. Vermersch, C. M. Fabre, G. L. Gattobigio, T. Lahaye, D. Guéry-Odelin, and R. Mathevet, "A Zeeman slower design with permanent magnets in a Halbach configuration," Review of Scientific Instruments **82**, 063115 (2011).

[47] Magnets manufactured by HKCM engineering - REF: 9964-61967.

[48] Magnets manufactured by HKCM engineering - REF: 9964-1799.

[49] K. Halbach, "Design of permanent multipole magnets with oriented rare earth cobalt material," Nuclear Instruments and Methods **169**, 1–10 (1980).

[50] T. Bergeman, G. Erez, and H. J. Metcalf, "Magnetostatic trapping fields for neutral atoms," Phys. Rev. A **35**, 1535–1546 (1987).

[51] J. S. Jackson and D. S. Durfee, "Magneto-Optical Trap Field Characterization with the Directional Hanle Effect," Sci Rep **9**, 8896 (2019).

[52] T. F. Gallagher, *Rydberg Atoms*, Cambridge Monographs on Atomic, Molecular and Chemical Physics (Cambridge University Press, Cambridge, 1994).

[53] A. Signoles, E. K. Dietsche, A. Facon, D. Grosso, S. Haroche, J. M. Raimond, M. Brune, and S. Gleyzes, "Coherent Transfer between Low-Angular-Momentum and Circular Rydberg States," Phys. Rev. Lett. **118**, 253603 (2017).

[54] D. A. Dahl, "Simion for the personal computer in reflection," International Journal of Mass Spectrometry Volume 200: The State of the Field as We Move into a New Millenium, **200**, 3–25 (2000).

[55] A. Derevianko, "Feasibility of Cooling and Trapping Metastable Alkaline-Earth Atoms," Phys. Rev. Lett. **87** (2001), 10.1103/PhysRevLett.87.023002.

[56] D. Sukachev, A. Sokolov, K. Chebakov, A. Akimov, N. Kolachevsky, and V. Sorokin, "Sub-doppler laser cooling of thulium atoms in a magneto-optical trap," Jetp Lett. **92**, 703–706 (2010).

[57] H. J. Metcalf and P. Van Der Straten, *Laser Cooling and Trapping*, edited by R. S. Berry, J. L. Birman, J. W. Lynn, M. P. Silverman, H. E. Stanley, and M. Voloshin, Graduate Texts in Contemporary Physics (Springer New York, New York, NY, 1999).

[58] T. Arpornthip, C. A. Sackett, and K. J. Hughes, "Vacuum-pressure measurement using a magneto-optical trap," Phys. Rev. A **85**, 033420 (2012).